HHS Public Access

Author manuscript

J Phys Chem Lett. Author manuscript; available in PMC 2018 January 16.

Published in final edited form as:

J Phys Chem Lett. 2017 November 16; 8(22): 5523–5530. doi:10.1021/acs.jpclett.7b02621.

MicroED structure of Au_{146}(p-MBA)$_{57}$ at subatomic resolution reveals a twinned FCC cluster

Sandra Vergara[1,‡], **Dylan A. Lukes**[2,‡], **Michael W. Martynowycz**[3,‡], **Ulises Santiago**[1], **German Plascencia-Villa**[1], **Simon C. Weiss**[2], **M. Jason de la Cruz**[3,#], **David M. Black**[1], **Marcos M. Alvarez**[1], **Xochitl Lopez-Lozano**[1], **Christopher O. Barnes**[2,†], **Guowu Lin**[2], **Hans-Christian Weissker**[4], **Robert L. Whetten**[1,*], **Tamir Gonen**[3,5,*], **Miguel Jose-Yacaman**[1,*], and **Guillermo Calero**[2,*]

[1]Department of Physics and Astronomy, The University of Texas at San Antonio, San Antonio, TX, USA.

[2]Department of Structural Biology, University of Pittsburgh, Pittsburgh, PA, USA.

[3]Janelia Research Campus, Howard Hughes Medical Institute, Ashburn, VA, USA.

[4]Aix Marseille Université, CNRS, CINaM UMR 7325, Marseille, France.

[5]Howard Hughes Medical Institute, Departments of Biological Chemistry and Physiology, David Geffen School of Medicine, University of California, Los Angeles, CA, USA.

Abstract

Solving the atomic structure of metallic clusters is fundamental to understanding their optical, electronic, and chemical properties. Herein we present the structure of the largest aqueous gold cluster, Au_{146}(p-MBA)$_{57}$ (p-MBA: *para*-mercaptobenzoic acid), solved by electron diffraction (MicroED) to subatomic resolution (0.85 Å) and by X-ray diffraction at atomic resolution (1.3 Å). The 146 gold atoms may be decomposed into two constituent sets consisting of 119 core and 27 peripheral atoms. The core atoms are organized in a twinned FCC structure whereas the surface gold atoms follow a C_2 rotational symmetry about an axis bisecting the twinning plane. The protective layer of 57 p-MBAs fully encloses the cluster and comprises bridging, monomeric, and dimeric staple motifs. Au_{146}(p-MBA)$_{57}$ is the largest cluster observed exhibiting a bulk-like FCC structure as well as the smallest gold particle exhibiting a stacking fault.

*Correspondence to: guc9@pitt.edu, tgonen@ucla.edu, robert.whetten@utsa.edu, Miguel.yacaman@utsa.edu.

†Present address: Division of Biology and Biological Engineering, California Institute of Technology, Pasadena, CA, USA.

#Present address: Structural Biology Program, Sloan Kettering Institute, Memorial Sloan Kettering Cancer Center, New York, NY, USA.

‡These authors contributed equally to this work.

ASSOCIATED CONTENT

Supporting Information. Crystallographic data summary, Mass Spectroscopy and DFT results. The following files are available free of charge.

Au146-PMB57.cif This file corresponds to X-ray Dataset 1 (SLS: XO6SA-PXI).

Au146-S17-PMB40.cif This file corresponds to X-ray Dataset 2 (APS: SERCAT-22ID)

Au146-S32-PMB25.cif This file corresponds to MicroED Dataset (Janelia: Titan Krios)

The authors declare no competing financial interests.

Keywords

Gold cluster; electron diffraction; single crystal X-ray; structure determination; stacking fault

Within the field of nanotechnology, metal clusters and nanoparticles are of central interest for their optical, electronic, and chemical properties. However, advances in this field have been limited by a lack of fidelity in the growth of nanoparticles. One strategy to achieve precise control over the shape and size of nanoparticles is the use of ligands as surface-protecting agents. This approach has enabled the synthesis of numerous stable clusters with atomically well-defined composition. Spectroscopic studies reveal that smaller metallic clusters have molecule-like electronic structures while larger ones support collective plasmon excitation similar to bulk-like nanoparticles [1–3]. Solving the atomic structure of protected metal clusters is fundamental to understanding their size-dependent properties. Single crystal X-ray diffraction (XRD) has previously revealed the structure of several thiolate-protected gold clusters [3–14]. Although some small clusters display FCC-like kernels [3–5], for several clusters –including the larger ones with {102, 130, 133, & 246} Au atoms– non-crystalline icosahedra and truncated decahedra (known as multiply twinned particles, or MTPs) have been found [11–14]. However, for sufficiently large clusters, a transition to bulk-like FCC packing should occur. Although some studies suggest a geometric and electronic transition occurring in the range of Au_{144} to Au_{329}, the critical size for this transition is not clear [1–2, 15–17]. Therefore, the case of ubiquitous clusters of ~29kDa core mass (1.7-nm core diameter), commonly identified as $Au_{144}(SR)_{60}$, is of particular interest. After two decades since this class of compounds was first reported [18], the precise composition and structure of the ~29kDa cluster remains elusive. The current models predict that $Au_{144}(SR)_{60}$ should have the icosahedral symmetry [19–20] whereas aqueous-phase samples may present polymorphism with competing icosahedral and truncated decahedral cores [21]. Unfortunately, structural efforts to reveal definitively its structure have thus far been unproductive. Herein we present a novel gold cluster in the ~29kDa size regime, $Au_{146}(SR)_{57}$, whose twinned-FCC structure departs from previous icosahedral and decahedral models proposed for $Au_{144}(SR)_{60}$.

Synthesis of the gold nanoclusters was achieved by a modified two-phase method [22], where clusters were precipitated by incubation in cold methanol or in cold methanol with 100mM ammonium acetate. The product was separated by native-PAGE (Figure S1). In both cases, analysis via liquid chromatography / high-resolution electrospray ionization mass spectroscopy (HPLC / ESI-MS) methods is consistent with the Au_{146}(p-MBA)$_{57}$ molecular formula (Figure S2). Thus, Au_{146}(p-MBA)$_{57}$ does not constitute an artifact of crystallization as it existed in solution prior to crystallization. Samples without ammonium acetate formed poorly-diffracting hexagonal plate crystals similar to those previously reported [21, 23–24], whereas samples co-precipitated with ammonium acetate crystallized as needles and plates in the presence of 25% polyethylene glycol 8000 and 50mM sodium potassium phosphate (Table S1). Large crystals as well as fragmented nanocrystals (Figure 1a) were selected for X-ray, free electron laser (FEL) or MicroED experiments [25–26], respectively. X-ray analysis provided resolution of 1.3 Å, while hardware limitations restricted FEL data to 1.7 Å only. Remarkably, subatomic resolution was only achieved with electron diffraction by MicroED

where crystals were analyzed in a frozen hydrated state by electron diffraction (Figures 1b and S3). A total of 146 gold atoms and 57 p-MBA ligands were identified in the electron density maps correlating with ESI-MS (Figure 1c). The surface representation of the metal cluster shows a globular and well-ordered structure that is effectively coated by p-MBA, preventing further growth (Figure 1d and Movie S1). The overall architecture of the cluster is illustrated stereographically by Figure 1e. The root-mean-square deviation between MicroED and X-ray atomic positions was 0.05 Å for the cluster kernel (innermost 13 Au atoms) and 0.1 Å for the entire gold structure, confirming the equivalence of the two methods. This MicroED structure represents the highest resolution structure for such aqueous phase gold clusters and the highest resolution reported to date by any cryoEM method.

The 146 gold atoms in the Au_{146}(p-MBA)$_{57}$ may be decomposed into two constituent sets: 119 core atoms and 27 peripheral atoms. The core atoms are organized in a twinned FCC structure (Figure 2a), whereas the surface gold atoms follow a C_2 rotational symmetry about an axis bisecting the twinning plane (Figure 2b). While FCC structures may be described morphologically as nested cuboctahedra, twinned FCC structures may be described as nested *anti*-cuboctahedra (Figure S4). Anti-cuboctahedra are also known as J27 under the Johnson solid classification system. The eight triangular faces of a J27 correspond to {111} planes, and the six square faces to {100} planes. The core of Au_{146}(p-MBA)$_{57}$ is comprised of three nested J27 shells: a first shell (J27-1) formed by the 12 immediate neighbors of the central Au-atom site, a second shell (J27-2) of 42 sites, and an incomplete third shell (J27-3) comprising 60 sites (115 in total). Two pairs of additional gold atoms located on {100} facets complete the 119-atom core. The observed truncation of 32 sites, with respect to an ideal J27-3 shell, rounds the morphology (Figure S5a–b), as these truncations occur at sites of low coordination-number: 12 at vertices, and 20 along edges (Figure S5c–h). In particular, sites on the boundary between mirror {111} planes are not occupied. In addition, in four of the {111} facets, we observe a lattice distortion that resembles the HCP packing. The occupied positions as well as the distorted positions in the third shell are symmetric across mirror planes. However, non-mirror {111} planes are distinct throughout the third shell. The view along the [111] direction (Figure 2c) shows that atoms belonging to J27-1 and J27-2 as well as the majority of atoms in J27-3 lie on the expected positions for an FCC, while most of the peripheral atoms deviate from ideal positions (Figures 2b and S6). The view along the [1–10] direction shows the twin in the Au_{146} structure.

Alternatively, one notes the presence of a 79-site twinned truncated octahedron (t-TO+) as a substructure of Au_{146} (Figure 2d). The superior stability of the Marks decahedron and t-TO+ was previously predicted for gold clusters as compared to the icosahedron or the untwinned TO+ [17, 27]. The 79-atom t-TO+ substructure may be recovered by capping each of the six {100} facets of J27-2 with four gold atoms. This t-TO+ also appears as a distinguishable group in the radial distance histogram from the central atom (Figure S7).

The protective layer of Au_{146}(p-MBA)$_{57}$ comprises 7 bridging motifs (-S-), 19 monomeric staple motifs (-S-Au-S-), and 4 dimeric staple motifs (-S-Au-S-Au-S-) arranged around the C_2 symmetry axis bisecting the twinning plane (Figure 3a–b). Four of the bridging motifs lie on {100} facets, two connect mirror {111} facets and one is located on the screw axis. This

bridging motif has been observed primarily on {100} facets [7, 10], but has recently been identified linking {111} facets in the structure of Au_{246}(p-MBT)$_{80}$ [14] (Figure S8). The monomeric staples connect adjacent facets. The four dimeric staples are anchored to {111} facets, two of them directly linked to atoms in the J27-2. Dimeric staples have been observed forming a "V" shape with the sulfur atoms in almost coplanar positions [9, 11]. In Au_{146}(p-MBA)$_{57}$, the three sulfur atoms (-S-Au-S-Au-S-) are not coplanar resulting in a bending of the staple. Interestingly, both characteristics of dimeric staples, the exclusive binding on {111} facets and the bending, are also present in the nonaqueous system Au_{246}(p-MBT)$_{80}$ [14] (Figure S8). The overall distribution of the staples is presented in Figure 3c.

Starting from the experimental coordinates we have analyzed the structure by density functional theory (DFT) methods. The optimized (relaxed) structure thus obtained retains all connectivity of the original, while removing much of its irregularities in interatomic distances, thereby enhancing the C_2-symmetry feature (Figure S9). In particular, Au-S bond lengths show a bimodal distribution, in agreement with experiment, where this double-peak structure is rather broad. The first peak is at 2.297 Å and corresponds to peripheral Au-S bonds, while the second is at 2.360 Å and corresponds to core Au-S bonds. We also observe a strong correlation between peaks of the radial distribution function and those of an FCC structure, with a peak gold-gold distance of 2.88 Å and most atoms in the range 2.73Å–3.1Å.

Gold clusters may manifest both crystalline FCC and non-crystalline structures. FCC cores have been observed in some small clusters [3–6, 8] and more recently, in the tetragonal-shaped Au_{92} [10]. Other clusters, including the larger ones (Au_{102}, Au_{130}, Au_{133}, and Au_{246}), display cores with five-fold symmetry (MTPs) [7, 9, 11–14]. Figure 4 shows the six largest gold clusters solved to date. Au_{92}[10] presents an FCC core; Au_{102}[11], Au_{130}[12], and Au_{246}[14] display decahedra cores; and Au_{133}[13] has a Mackay icosahedral core. Au_{146} is the largest solved cluster with a FCC core. In addition, it is the smallest gold nanoparticle observed containing a stacking fault. These planar defects are very common in much larger particles (such as colloidal gold) but have never been observed at this low number of atoms.

Although icosahedral and decahedral structures display energetically-favorable close-packed outer facets, as the size of the particle increases, a preference for bulk-like FCC structures is expected. While nucleation mechanisms remain unclear, most likely FCC nanoparticles should grow starting from FCC seeds. The favorability of a cluster as a seed for an FCC particle is linked to the ability to grow quickly and leave the subcritical size region before disintegration [28]. The twinned-FCC anti-cuboctahedral kernel of Au_{146} may therefore be a more suitable seed than a cuboctahedral kernel, as the saturation of {100} facets in J27 generates extra sites with 4-coordination on the twin plane than are absent in the untwinned structure (Figure S10). This creation of 4-coordination sites is similar to the well-established effect of twins in the growth of nanoparticles [29]. In the case of nanoparticles, the introduction of twins favors a kinetic growth on the twin that leads to thermodynamically-unfavorable shapes like triangular plates or rods in a similar fashion that screw dislocations favor the growth of large crystals [30].

In this report we have shown that even a FCC structure with such few atoms (Au146, ~1.7 nm) contains a well-defined twinning plane. Considering that decahedral structures have 5 twin-planes and icosahedra have 30 twin-planes, twinning appears to be a critical component of nanoparticle structure from a very early stage of growth. Moreover, to our knowledge, the subatomic resolution structure of Au_{146}(p-MBA)$_{57}$ presented here is the first such structure of a metal cluster obtained by electron diffraction of frozen hydrated samples, establishing MicroED as a new and important tool for the characterization of nanomaterials.

EXPERIMENTAL METHODS

Synthesis and Purification of Gold Nanoclusters

The gold nanoclusters were produced by the two-phase method with some minor modifications [23, 31–33]. First, stock solution of *para*-mercaptobenzoic acid (p-MBA) at 100 mM was prepared in 300 mM NaOH by vigorous stirring for at least 3 h or overnight and pulsed sonication. Nanoclusters were typically produced in 25 ml batches in 50 % v/v methanol in a 50 ml round flask by adding aqueous $HAuCl_4$ to a final concentration of 3 mM and p-MBA to 9 mM. The color of this solution was light yellow. The mixture was stirred overnight until solution was almost clear/colorless. Then freshly prepared ice-cold aqueous $NaBH_4$ was added to achieve 1.5 mM final concentration, and the reaction proceeded for 2 h. The entire content was transferred to a 50 ml conical tube. Volume was completed to 50 ml with cold methanol. Two distinct approaches were used to precipitate the as-prepared cluster product: cold methanol or cold methanol with 100 mM ammonium acetate. The content was mixed gently and incubated at 4°C. Nanoclusters were concentrated with centrifugation at 2000–3000 rpm for15 min, supernatant removed, and the pellet resuspended in 25 ml methanol. Nanoclusters were again concentrated by centrifugation at 2000–3000 rpm for 15 min, supernatant removed, and the pellet air dried. Finally, the pellet was dissolved in a small volume with ultrapure ddH_2O (0.5–1 ml). Product quality was assessed by native 10–12 % PAGE in TBE buffer at 100 V. Major bands corresponding to gold nanoclusters were cut from the gel to separate the fractions of interest and then re-concentrated by precipitation with methanol or rotary evaporator. Aliquots in ultrapure ddH_2O were stored at 4°C for further analysis. Stability of gold nanoclusters in both samples, with and without ammonium acetate coprecipitation, was monitored by routine 10–12 % PAGE, UV-Vis and Transmission Electron Microscopy (TEM), confirming no perceivable changes over 6 months.

Gold cluster crystallization

The two cluster samples, with and without ammonium acetate coprecipitation, were submitted to crystallization screenings. The sample without ammonium acetate formed poorly-diffracting hexagonal plates, whereas the sample coprecipitated with ammonium acetate crystallized in the presence of 25% polyethylene glycol 8000 (PEG8K) and 50 mM sodium potassium phosphate. Crystals were transferred to a stabilizing solution for cryo-protection containing 25% methyl pentanediol (MPD), 5% PEG 8K and 50mM sodium potassium phosphate.

Electron Micro-Diffraction (MicroED)

Crystals were too big for MicroED thus a fragmentation protocol was designed [34]. Crystals in stabilizing solution (see above) were harvested in a 0.5 ml Eppendorf tube and 30 mgs of stainless steel beads (1 mm diameter) were placed for fragmentation [35–36]. Sample was vortexed several times and the presence of homogeneously sized fragments was verified using bright field microscopy. Stainless steel beads were removed using a magnet and samples were centrifuged at 1000 rpms to pellet the fragments. Excess of mother liquour was removed to obtain a concentrated slurry and stabilizing cryo-protecting solution was added and mixed carefully with the slurry. This procedure was repeated three times to ensure full buffer exchange. Holey 300 mesh carbon Quantifoil® R2/2 grids were negatively glow discharged at 25 mA and 2*10^-1 mbar for 30s from both sides. Then 2 μl of the concentrated and cryoprotected nanocrystal solution were pipetted onto the grid and incubated for 1 minute, before the excess liquid was removed by careful blotting from the backside using Fisherbrand P2 filter paper. Afterwards the grid was flash frozen by plunging it into liquid nitrogen. The grids were stored in liquid nitrogen until they were used for data collection.

MicroED Data were collected using an FEI Titan Krios TEM equipped with a field emission gun operating at 300kV, corresponding to an electron wavelength of 0.0197Å [25–26]. Data was recorded with a TVIPS TemCam-F416 4K × 4K CMOS camera with sensor pixel dimensions of 15.6 μm × 15.6 μm. Images were taken in rolling-shutter mode with 2X-pixel binning, resulting in final images of 2048 px × 2048 px. Frames were acquired under a continuous rotation of 0.1°/s every 5 s, or a 0.5° wedge of reciprocal space per frame. Data was converted using open-source software and corrected for pixel truncation as previously described [37–38]. MicroED experiments were performed at liquid nitrogen temperatures, ~77K. Nano crystals diffracted to 0.7Å resolution by MicroED.

Structure Refinement

X-ray and MicroED data were processed in space group P1 using the software package XDS [39]. Reflections were indexed using the program XPREP in P2(1)/n or P2(1)/c. The X-ray structure was solved using the program SHELXT [40] yielding 146 gold and 57 sulfur atoms. The Fo-Fc difference map using X-ray data set 2 (Table S1) showed positive density for forty pMBA molecules. The full model was completed using the difference map (Fo-Fc) from X-ray data set 1 (Table S1) which revealed all fifty-seven pMBA molecules (Figure S3c–d). The MicroED structure was solved using a partial solution obtained with the program Shake and Bake [41] where 79 Au atoms were clearly identified in the Patterson map. The remaining Au atoms and all 57 sulfurs were easily identified as positive density in the Fo-Fc map. Only a few p-MBA molecules were observed in the MicroED data.

The MicroED and X-ray structures were refined using the programs SHELXL [42] and Phenix [43]. Several rounds of manual building and refinement were employed to place the pMBA molecules.

Mass Spectrometry

Samples were analyzed by HPLC-ESI-ToF-MS. The LC-MS method resolves (separates) multi-component samples (chromatographically) prior to the identification of each component (mass-spectrometrically), reducing interference from adducts [44–45]. $Au_{102}(pMBA)_{44}$ clusters were used for validation of the quality of the technique. The Au_{146} clusters were detected intact. The major peak could be cleanly attributed to the intact (146,57) species, in the charge-states = [4-] thru [7-], with [5-] dominant. Minor satellite peaks could be attributed to water adduction.

Computational DFT methods

The *ab initio* DFT structural optimization started from the experimental structure. Subsequently, the structure was relaxed using the VASP code [46–47] with PAWs until all forces were smaller than 0.02 eV/ Å. An energy cutoff of 280 eV was employed. A charge state of 3- (three additional electrons) was used to comply with the expected electronic shell closing at 2008 electrons according to the superatom model. Among our various optimizations with distinct exchange-correlation functionals, ligand models (SR: Cl-, R:CH_3, or SR:pMBA), and charge states {3+, 1+, 1−, 3−}, the LDA optimization chg.= 3- turns out to best represent the Au-Au bonds, unlike the calculations done using a GGA functional (PBE; not shown), to which the missing hydrogen atoms were added.

Supplementary Material

Refer to Web version on PubMed Central for supplementary material.

Acknowledgments

We would like to acknowledge May Elizabeth Sharp and Meitan Wang at the Swiss Light Source (SLS). We would also like to acknowledge Michael Becker and Craig Ogata at GM/CA (Argonne National Laboratory). We would also like to acknowledge John Chrzas and Rod Salazar at the South East Regional Collaborative Access Team (SERCAT, Argonne National Laboratory). The authors acknowledge Aina Cohen and Jinhu Song, from the Macromolecular Femtosecond Crystallography (MFX) at the Linac Coherent Light Source (LCLS) for their support during data collection. We thank D. Lee for home-source X-ray technical support at the University of Pittsburgh. Research reported in this publication was supported by the National Institute on Minority Health and Health Disparities (NIMHD) of the National Institutes of Health (#G12-MD007591) and by The Welch Foundation grants #AX-1615 and #AX-1857. GC acknowledges University of Pittsburgh startup funds and support from NIH grants P50-GM082251, R01-GM112686 and BioXFEL-STC1231306. GM/CA@aps has been funded in whole or in part with Federal funds from the National Cancer Institute (ACB-12002) and the National Institute of General Medical Sciences (AGM-12006). Use of the Advanced Photon Source was supported by the U. S. Department of Energy, Office of Science, Office of Basic Energy Sciences, under Contract No. W-31-109-Eng-38. Use of the Linac Coherent Light Source (LCLS), SLAC National Accelerator Laboratory, is supported by the U.S. Department of Energy, Office of Science, Office of Basic Energy Sciences under Contract No. DE-AC02-76SF00515. The Gonen laboratory is supported by the Howard Hughes Medical Institute and this work was also supported by the Janelia Research Campus visitor program. The contents of this publication are solely the responsibility of the authors and do not necessarily represent the official views of NIGMS or NIH.

References

1. Negishi Y, Nakazaki T, Malola S, Takano S, Niihori Y, Kurashige W, Yamazoe S, Tsukuda T, Hakkinen H. A Critical Size for Emergence of Nonbulk Electronic and Geometric Structures in Dodecanethiolate-Protected Au Clusters. J. Am. Chem. Soc. 2015; 137:1206–12. [PubMed: 25549276]
2. Zhou M, Zeng CJ, Chen YX, Zhao S, Sfeir MY, Zhu MZ, Jin RC. Evolution from the Plasmon to Exciton State in Ligand-Protected Atomically Precise Gold Nanoparticles. Nat. Commun. 2016; 7

3. Zeng C, Chen Y, Iida K, Nobusada K, Kirschbaum K, Lambright KJ, Jin R. Gold Quantum Boxes: On the Periodicities and the Quantum Confinement in the Au(2)(8), Au(3)(6), Au(4)(4) , and Au(5)(2) Magic Series. J. Am. Chem. Soc. 2016; 138:3950–3. [PubMed: 26934618]
4. Zeng C, Li T, Das A, Rosi NL, Jin R. Chiral Structure of Thiolate-Protected 28-Gold-Atom Nanocluster Determined by X-Ray Crystallography. J. Am. Chem. Soc. 2013; 135:10011–3. [PubMed: 23815445]
5. Zeng C, Qian H, Li T, Li G, Rosi NL, Yoon B, Barnett RN, Whetten RL, Landman U, Jin R. Total Structure and Electronic Properties of the Gold Nanocrystal Au36(Sr)24. Angew. Chem. Int. Ed. 2012; 51:13114–13118.
6. Crasto D, Malola S, Brosofsky G, Dass A, Hakkinen H. Single Crystal Xrd Structure and Theoretical Analysis of the Chiral Au30s(S-T-Bu)18 Cluster. J. Am. Chem. Soc. 2014; 136:5000–5. [PubMed: 24605935]
7. Qian H, Eckenhoff WT, Zhu Y, Pintauer T, Jin R. Total Structure Determination of Thiolate-Protected Au38 Nanoparticles. J. Am. Chem. Soc. 2010; 132:8280–1. [PubMed: 20515047]
8. Yang S, Chai J, Song Y, Kang X, Sheng H, Chong H, Zhu M. A New Crystal Structure of Au36 with a Au14 Kernel Cocapped by Thiolate and Chloride. J. Am. Chem. Soc. 2015; 137:10033–5. [PubMed: 26252023]
9. Heaven MW, Dass A, White PS, Holt KM, Murray RW. Crystal Structure of the Gold Nanoparticle [N(C8h17)4][Au25(Sch2ch2ph)18]. J. Am. Chem. Soc. 2008; 130:3754–5. [PubMed: 18321116]
10. Zeng C, Liu C, Chen Y, Rosi NL, Jin R. Atomic Structure of Self-Assembled Monolayer of Thiolates on a Tetragonal Au92 Nanocrystal. J. Am. Chem. Soc. 2016; 138:8710–3. [PubMed: 27355843]
11. Jadzinsky PD, Calero G, Ackerson CJ, Bushnell DA, Kornberg RD. Structure of a Thiol Monolayer-Protected Gold Nanoparticle at 1.1 a Resolution. Science. 2007; 318:430–3. [PubMed: 17947577]
12. Chen Y, Zeng C, Liu C, Kirschbaum K, Gayathri C, Gil RR, Rosi NL, Jin R. Crystal Structure of Barrel-Shaped Chiral Au130(P-Mbt)50 Nanocluster. J. Am. Chem. Soc. 2015; 137:10076–9. [PubMed: 26244606]
13. Zeng C, Chen Y, Kirschbaum K, Appavoo K, Sfeir MY, Jin R. Structural Patterns at All Scales in a Nonmetallic Chiral Au(133)(Sr)(52) Nanoparticle. Sci. Adv. 2015; 1:e1500045. [PubMed: 26601152]
14. Zeng C, Chen Y, Kirschbaum K, Lambright KJ, Jin R. Emergence of Hierarchical Structural Complexities in Nanoparticles and Their Assembly. Science. 2016; 354:1580–1584. [PubMed: 28008066]
15. Philip R, Chantharasupawong P, Qian HF, Jin RC, Thomas J. Evolution of Nonlinear Optical Properties: From Gold Atomic Clusters to Plasmonic Nanocrystals. Nano Lett. 2012; 12:4661–4667. [PubMed: 22845756]
16. Yi C, Zheng H, Tvedte LM, Ackerson CJ, Knappenberger KL. Nanometals: Identifying the Onset of Metallic Relaxation Dynamics in Monolayer-Protected Gold Clusters Using Femtosecond Spectroscopy. J. Phys. Chem. C. 2015; 119:6307–6313.
17. Cleveland CL, Landman U, Schaaff TG, Shafigullin MN, Stephens PW, Whetten RL. Structural Evolution of Smaller Gold Nanocrystals: The Truncated Decahedral Motif. Phys. Rev. Lett. 1997; 79:1873–1876.
18. Whetten RL, Khoury JT, Alvarez MM, Murthy S, Vezmar I, Wang Z, Stephens PW, Cleveland CL, Luedtke W, Landman U. Nanocrystal Gold Molecules. Adv. Mater. 1996; 8:428–433.
19. Lopez-Acevedo O, Akola J, Whetten RL, Grönbeck H, Häkkinen H. Structure and Bonding in the Ubiquitous Icosahedral Metallic Gold Cluster Au 144(Sr) 60. J. Phys. Chem. C. 2009; 113:5035–5038.
20. Bahena D, Bhattarai N, Santiago U, Tlahuice A, Ponce A, Bach SBH, Yoon B, Whetten RL, Landman U, Jose-Yacaman M. Stem Electron Diffraction and High-Resolution Images Used in the Determination of the Crystal Structure of the Au144(Sr)60 Cluster. J. Phys. Chem. Lett. 2013; 4:975–981. [PubMed: 23687562]

21. Jensen KM, Juhas P, Tofanelli MA, Heinecke CL, Vaughan G, Ackerson CJ, Billinge SJ. Polymorphism in Magic-Sized Au144(Sr)60 Clusters. Nat. Commun. 2016; 7:11859. [PubMed: 27297400]
22. Plascencia-Villa G, Demeler B, Whetten RL, Griffith WP, Alvarez M, Black DM, Jose-Yacaman M. Analytical Characterization of Size-Dependent Properties of Larger Aqueous Gold Nanoclusters. J. Phys. Chem. C. 2016; 120:8950–8958.
23. Mustalahti S, Myllyperkiö P, Lahtinen T, Salorinne K, Malola S, Koivisto J, Häkkinen H, Pettersson M. Ultrafast Electronic Relaxation and Vibrational Cooling Dynamics of Au144(Sc2h4ph)60 Nanocluster Probed by Transient Mid-Ir Spectroscopy. J. Phys. Chem. C. 2014; 118:18233–18239.
24. Wong OA, Heinecke CL, Simone AR, Whetten RL, Ackerson CJ. Ligand Symmetry-Equivalence on Thiolate Protected Gold Nanoclusters Determined by Nmr Spectroscopy. Nanoscale. 2012; 4:4099–102. [PubMed: 22543449]
25. Shi D, Nannenga BL, Iadanza MG, Gonen T. Three-Dimensional Electron Crystallography of Protein Microcrystals. Elife. 2013; 2:e01345. [PubMed: 24252878]
26. Nannenga BL, Shi D, Leslie AG, Gonen T. High-Resolution Structure Determination by Continuous-Rotation Data Collection in Microed. Nat. Methods. 2014; 11:927–30. [PubMed: 25086503]
27. Doye JPK, Wales DJ. Structural Consequences of the Range of the Interatomic Potential - a Menagerie of Clusters. J. Chem. Soc. Faraday T. 1997; 93:4233–4243.
28. Vandewaal BW. An Atomic-Scale Model of Fcc Crystal-Growth. Z. Phys. D Atom. Mol. Cl. 1991; 20:349–352.
29. Lofton C, Sigmund W. Mechanisms Controlling Crystal Habits of Gold and Silver Colloids. Adv. Funct. Mater. 2005; 15:1197–1208.
30. Burton WK, Cabrera N, Frank FC. The Growth of Crystals and the Equilibrium Structure of Their Surfaces. Philos. Trans. R. Soc. London, Ser. A. 1951; 243:299.
31. Alvarez MM, Chen J, Plascencia-Villa G, Black DM, Griffith WP, Garzon IL, Jose-Yacaman M, Demeler B, Whetten RL. Hidden Components in Aqueous "Gold-144" Fractionated by Page: High-Resolution Orbitrap Esi-Ms Identifies the Gold-102 and Higher All-Aromatic Au-Pmba Cluster Compounds. J. Phys. Chem. B. 2016; 120:6430–6438. [PubMed: 27275518]
32. Tvedte LM, Ackerson CJ. Size-Focusing Synthesis of Gold Nanoclusters with P-Mercaptobenzoic Acid. J. Phys. Chem. A. 2014; 118:8124–8128. [PubMed: 24628255]
33. Heinecke, CL., Ackerson, CJ. Preparation of Gold Nanocluster Bioconjugates for Electron Microscopy. In: Sousa, AA., Kruhlak, MJ., editors. Nanoimaging: Methods and Protocols. Humana Press; Totowa, NJ: 2013. p. 293-311.
34. de la Cruz MJ, et al. Atomic-Resolution Structures from Fragmented Protein Crystals with the Cryoem Method Microed. Nat. Methods. 2017; 14:399–402. [PubMed: 28192420]
35. Stevenson HP, et al. Transmission Electron Microscopy for the Evaluation and Optimization of Crystal Growth. Acta. Crystallogr. D Struct. Biol. 2016; 72:603–15. [PubMed: 27139624]
36. Barnes CO, Kovaleva EG, Fu X, Stevenson HP, Brewster AS, DePonte DP, Baxter EL, Cohen AE, Calero G. Assessment of Microcrystal Quality by Transmission Electron Microscopy for Efficient Serial Femtosecond Crystallography. Arch. Biochem. Biophys. 2016; 602:61–8. [PubMed: 26944553]
37. Hattne J, Shi D, de la Cruz MJ, Reyes FE, Gonen T. Modeling Truncated Pixel Values of Faint Reflections in Microed Images. J. Appl. Crystallogr. 2016; 49:1029–1034. [PubMed: 27275145]
38. Hattne J, Reyes FE, Nannenga BL, Shi D, de la Cruz MJ, Leslie AG, Gonen T. Microed Data Collection and Processing. Acta Crystallogr. A Found. Adv. 2015; 71:353–60. [PubMed: 26131894]
39. Kabsch W. Xds. Acta Crystallogr. D Biol. Crystallogr. 2010; 66:125–32. [PubMed: 20124692]
40. Sheldrick GM. Shelxt - Integrated Space-Group and Crystal-Structure Determination. Acta Crystallogr. A Found. Adv. 2015; 71:3–8. [PubMed: 25537383]
41. Miller R, Gallo SM, Khalak HG, Weeks CM. Snb - Crystal-Structure Determination Via Shake-and-Bake. J. Appl. Crystallogr. 1994; 27:613–621.

42. Sheldrick GM. A Short History of Shelx. Acta Crystallogr A. 2008; 64:112–22. [PubMed: 18156677]

43. Adams PD, et al. Phenix: A Comprehensive Python-Based System for Macromolecular Structure Solution. Acta Crystallogr. D Biol. Crystallogr. 2010; 66:213–221. [PubMed: 20124702]

44. Black DM, Bach SB, Whetten RL. Capillary Liquid Chromatography Mass Spectrometry Analysis of Intact Monolayer-Protected Gold Clusters in Complex Mixtures. Anal. Chem. 2016; 88:5631–6. [PubMed: 27216373]

45. Black DM, Alvarez MM, Yan F, Griffith WP, Plascencia-Villa G, Bach SBH, Whetten RL. Triethylamine Solution for the Intractability of Aqueous Gold–Thiolate Cluster Anions: How Ion Pairing Enhances Esi-Ms and Hplc of Aq-Aun(Pmba)P. J. Phys. Chem. C. 2016

46. Kresse G, Furthmüller J. Efficiency of Ab-Initio Total Energy Calculations for Metals and Semiconductors Using a Plane-Wave Basis Set. Comp. Mater. Sci. 1996; 6:15–50.

47. Kresse G, Joubert D. From Ultrasoft Pseudopotentials to the Projector Augmented-Wave Method. Phys. Rev. B. 1999; 59:1758–1775.

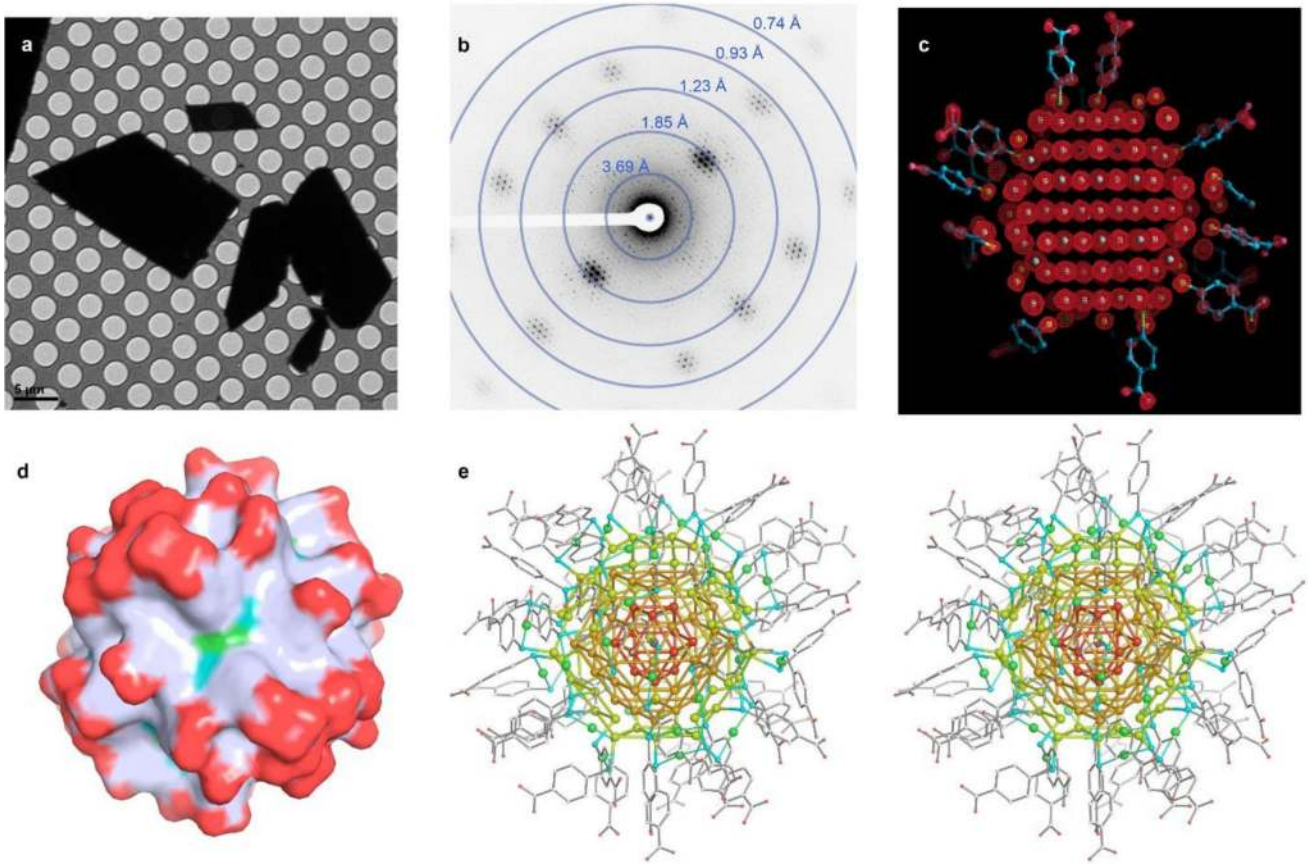

Figure 1.

MicroED and X-ray determination of the crystal structure of $Au_{146}(p\text{-}MBA)_{57}$. **a**, Transmission electron micrograph of $Au_{146}(p\text{-}MBA)_{57}$ crystals, and **b**, typical MicroED data extending well beyond 1Å. **c**, MicroED density map (2Fo-Fc, contoured at 2 σ) shown as red mesh, identifies atomic positions of Au (white spheres) and S (yellow spheres) atoms. Ligands (p-MBA) are shown as blue framework. **d**, Surface representation of the cluster with oxygen in red, carbon in white, sulfur in cyan, and gold in green. The full set of p-MBA ligands was determined using X-ray data. **e**, Stereoscopic representation of the cluster including all gold atoms and p-MBA ligands. Gold atoms colored by shells for visualization purposes (see Figure 2).

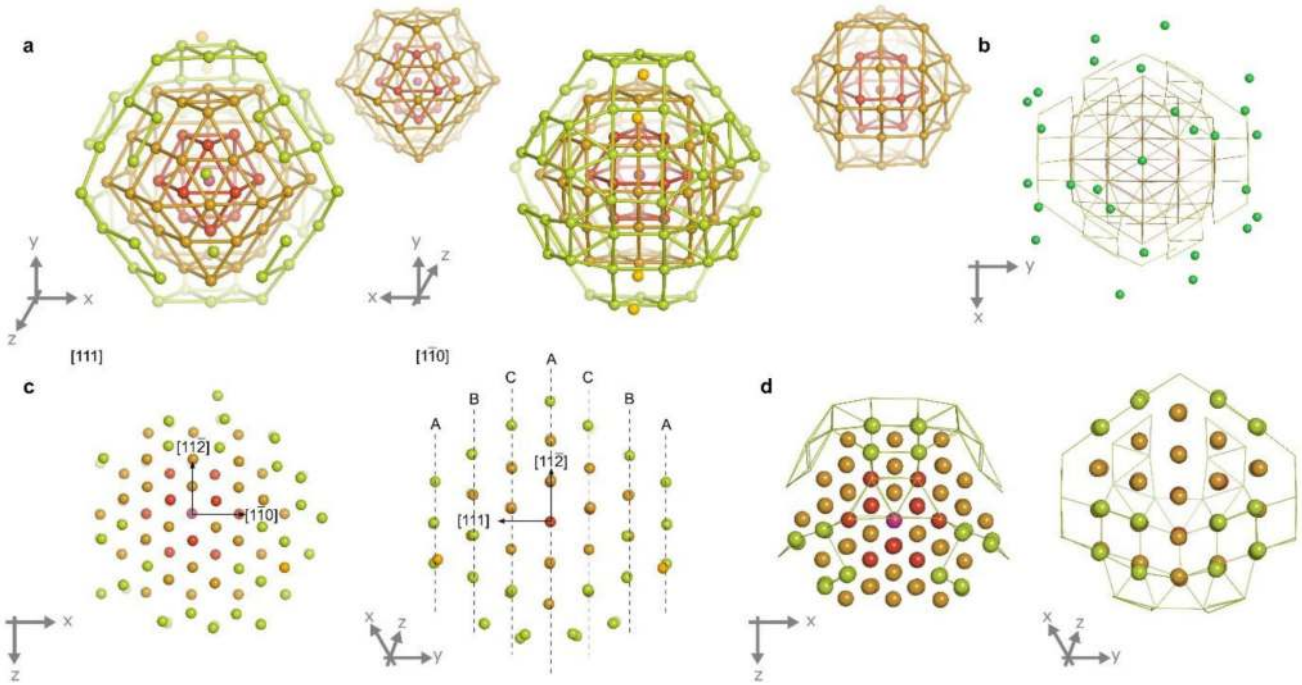

Figure 2.

Configuration of gold atoms in $Au_{146}(p\text{-}MBA)_{57}$. **a**, Core structure (119-atoms) of the Au_{146} cluster. The central atom, purple, and the first shell J27-1, red, comprise the kernel of the cluster; second shell J27-2, brown; third shell J27-3, light green; extra atoms in the core, dark yellow. Twin plane parallel to xz-plane. **b**, Location of peripheral gold atoms (27-atoms) in dark green, with core displayed in wires. **c**, View of crystallographic planes. Plane directions are absolute to an FCC unit cell. **d**, Selection of 79-atom corresponding to a twinned truncated octahedron, t-TO+. Remaining atoms from core displayed on wires.

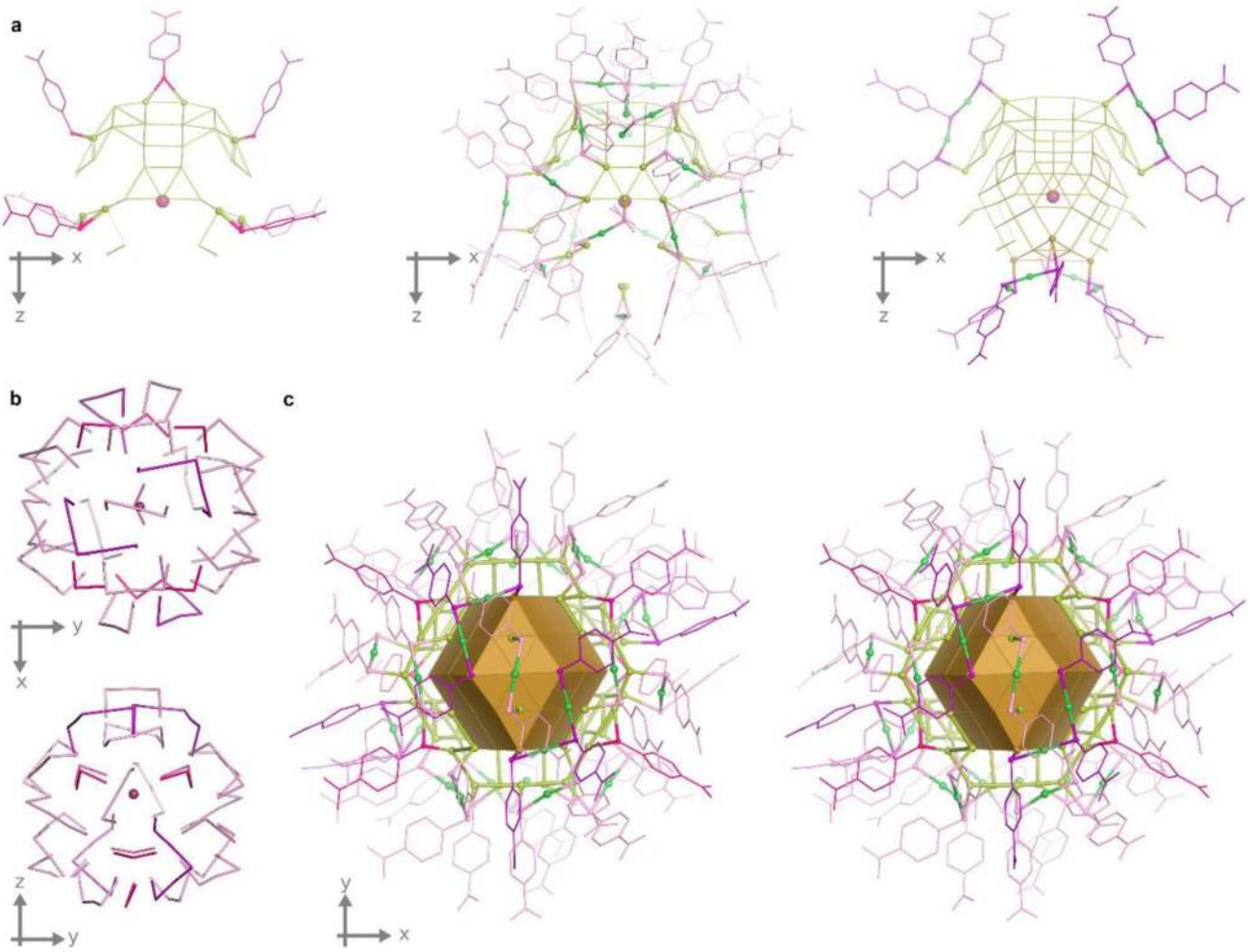

Figure 3.

Configuration of ligands (p-MBA) on Au146(p-MBA)57. **a**, Distribution of the three types of staples on the core surface of Au146(p-MBA)57. Bridging motifs (left) in pink, monomeric staples (center) in light pink, and dimeric staples (right) in purple. **b**, Rotational symmetric distribution of staples. Screw axis parallel to z-axis bisecting the twin plane (xz-plane). **c**, Stereoscopic view of Au146(p-MBA)57 displaying all different types of staples, J27-2 atoms are displayed as solid surface.

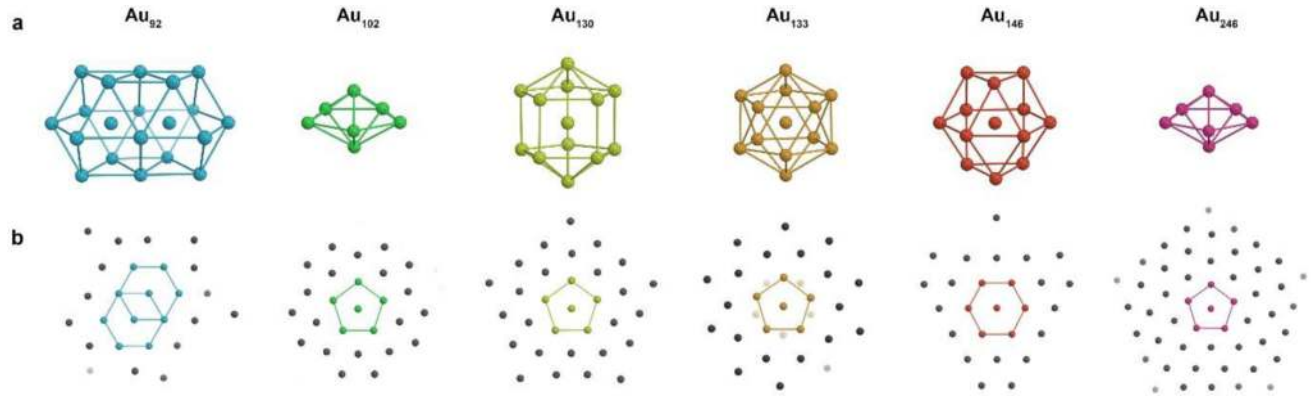

Figure 4.

Atomic structures of the largest gold clusters solved to date. **a**, Kernel structures of Au_{92} (conjoined cuboctahedra with no unique central atom); Au_{102} and Au_{246} (decahedra); Au_{130} (Ino decahedron); Au_{133} (icosahedron); and Au_{146} (anti-cuboctahedron). **b**, The view along the [111] axis for Au_{92} and Au_{146} shows the atomic positions following the close-packing of FCC structures, whereas the projection along [110] axis for Au_{102}, Au_{130}, Au_{133}, and Au_{246} shows five-fold symmetry.